

~~CONFIDENTIAL~~Copy 6
RM E53B09

NACA RM E53B09



RESEARCH MEMORANDUM

DESIGN PROCEDURE AND LIMITED TEST RESULTS FOR A HIGH
SOLIDITY, 12-INCH TRANSONIC IMPELLER
WITH AXIAL DISCHARGE

By Linwood C. Wright and Karl Kovach

Lewis Flight Propulsion Laboratory
Cleveland, Ohio

CLASSIFICATION CHANGED

To UNCLASSIFIED

NACA Red also
By authority of *4 RN-125* Date *effective*
Feb 26, 1958
ADP 3-20 18

CLASSIFIED DOCUMENT

This material contains information affecting the National Defense of the United States within the meaning of the espionage laws, Title 18, U.S.C., Secs. 793 and 794, the transmission or revelation of which in any manner to an unauthorized person is prohibited by law.

NATIONAL ADVISORY COMMITTEE FOR AERONAUTICS

WASHINGTON

April 9, 1953

~~CONFIDENTIAL~~

NATIONAL ADVISORY COMMITTEE FOR AERONAUTICS

RESEARCH MEMORANDUMDESIGN PROCEDURE AND LIMITED TEST RESULTS FOR A HIGH SOLIDITY, 12-INCH
TRANSONIC IMPELLER WITH AXIAL DISCHARGE

By Linwood C. Wright and Karl Kovach

SUMMARY

An approximate inverse impeller design procedure based on the assumption of axisymmetric, nonviscous flow is presented along with some limited experimental data obtained from a high solidity, 12-inch transonic impeller. The design procedure consists of a point-by-point solution of the impeller flow conditions along a series of streamlines in the radial-axial plane. Also, a method is presented for estimating the blade loading from the moment of momentum considerations when the mean channel flow is assumed parallel to the mean blade surface and the static pressure is assumed to vary linearly across the passage.

The transonic impeller designed for an equivalent tip speed of 1200 feet per second by means of the subject procedure consists of a 0.40 hub-tip ratio, swept-back leading edge, aluminum-bladed rotor.

The design performance was not obtained experimentally because of a restriction of the flow in the outlet annulus downstream of the impeller which causes the flow to be about 14 percent less than the design value. The resulting large angles of attack at the blade leading edges caused vibrations which induced partial structural failure before alteration of the outlet passage could be accomplished. After the initial partial fracture of one of the blades, total failure was delayed by installation of damping wires threaded through the blades. Although further running time could be obtained by use of damping wires, the life of this configuration was too short to justify extensive alteration of the outlet in order to alleviate the choking.

Because the flow was choked in the outlet annulus, at design equivalent tip speed the experimental performance was restricted to a pressure ratio of 2.164 at an equivalent weight flow of 26.47 pounds per second (33.71 lb/sec-sq ft of frontal area) and an impeller adiabatic efficiency of 81 percent.

The impeller was designed to have a static-pressure drop from inlet to exit in order to reduce the adverse viscous effects. However, the losses due to resulting high stator inlet Mach numbers are concluded to

outweigh any favorable effects on the boundary layer. Also, the advisability of approaching equal energy input along the blade span is indicated.

INTRODUCTION

For some time compressor designers were of the opinion that the performance of axial-flow compressors would be limited by a maximum blade relative Mach number. The belief existed that after the fashion of isolated subsonic airfoils, performance deteriorated rapidly once the blade relative speeds approached the critical or force-break values (ref. 1). Experiments indicated that this belief was reasonably accurate for the conventional airfoil sections and rotor configurations utilized in subsonic axial-flow compressors.

One-dimensional analysis of supersonic flow configurations indicated that if the extended bow wave pattern observed when subsonic blading was placed in a supersonic stream could be eliminated and the normal shock confined within the passage, then reasonable efficiencies and considerably increased pressure ratios might be realized. The proposed method for eliminating the extended wave pattern incorporated the earlier principle of the Busemann biplane to contain the wave system wholly within the blade passage. This requirement led to the necessity of maintaining the entrance relative Mach number sufficiently large to allow passage of all of the flow for the given blade contraction without spillage (refs. 2 and 3).

Early supersonic compressors were designed with the idea of meticulously avoiding blade relative hub Mach numbers below those which would permit shock entrance at design speed along the entire blade span. This restriction placed a limit on the minimum hub-tip radius ratio for a given inlet velocity and rotational speed and hence limited the maximum weight flow. This minimum Mach number restriction led to the use of relatively high tip speeds (usually about 1500 or 1600 ft/sec) and the attendant severe structural problem. Moreover, attention was focused away from the intermediate tip speed range (1100 to 1400 ft/sec) where reasonable radius ratios and resulting large weight flows were structurally feasible. This speed range was avoided because the resultant relative Mach numbers fell in the transonic speed range where the extended wave pattern could be neither eliminated nor analyzed.

Experimental results of several supersonic compressors, however, indicated that their performance in the speed range described as transonic (1100 to 1400 ft/sec) was in general better than the design speed performance (see refs. 4 and 5). The discontinuous variation in flow conditions with speed which might have been expected (at the speed of shock entry) was not observed. There was evidence that large losses

CONFIDENTIAL

were not inherent in working with transonic flows. In the absence of viscous wall effects this might have been readily predicted inasmuch as the shock losses are inherently small.

The above observations led to consideration of the transonic compressor configuration which is characterized by subsonic blade inlet relative velocities at the hub and supersonic blade inlet relative velocities at the tip at rated speed. The configuration is such that arbitrarily low hub-tip radius ratios may be utilized with greatly increased weight flow per unit frontal area. The theoretical pressure ratio per stage generally can exceed considerably that of a subsonic stage while falling somewhat below that of a supersonic stage. The efficiency will theoretically exceed that of a supersonic stage but probably cannot equal that of a subsonic stage of optimum design. The generally reduced tip speed allows the use of increased blade span for a given stress level.

Thus, an analytical and experimental investigation of the compressor type termed transonic was undertaken for the purpose of developing an appropriate design procedure, designing, testing, and analyzing the performance of a high solidity transonic impeller. This impeller differs from the axial-flow transonic impeller of reference 6 primarily in that the current impeller utilizes a lower hub-tip ratio, more turning, a considerably higher solidity, and a decreasing mean static pressure through the impeller. The accelerating mean flow was intended to prevent large boundary layer growths and eliminate the necessity for large boundary layer allowances to prevent choking. A necessary consequence, however, is the undesirably high Mach number level of the impeller absolute leaving flow.

This report presents the transonic impeller design procedure and limited test results. The experimental results are incomplete because of inability of the test rig to pass the design weight flow and are insufficient to warrant strong conclusions regarding the questionable advantages of an accelerating mean flow through the rotor. The occurrence of structural failure did not allow sufficient time to make the changes in the exit flow passage which would have been required to permit passage of the design flow.

DESIGN PROCEDURE

The first objective of the program was the development of a design procedure. Complete freedom in the aerodynamic specifications would be highly desirable; however, for the desired configuration of relatively high wheel speed and long blade height, structural considerations will necessarily restrict the aerodynamic freedom.

In order to control centrifugal stresses, specification of the radial distribution of blade thickness should be allowed. In addition, radial blade elements will be desirable to eliminate excessive bending stresses. The only remaining freedom that is available to satisfy aerodynamic specifications is then the blade mean line angle and thickness distribution along a single streamline or specified contour in the radial-axial plane. The design procedure under these conditions reduces to two parts: (1) The selection of the blade shape and thickness distribution along a given streamline, and (2) the determination of the rotor hub and tip annular boundaries that permits the required weight flow to pass through the impeller compatible with the desired conditions existing on the specified streamline. The remaining portion of the blade other than the specified section will be fixed by the condition of radial blade elements and a specified radial taper.

The procedure herein described is usually designated as the inverse procedure in compressor design practice. That is, the tip speed and performance are specified and the necessary impeller geometry is determined.

Simplifying Assumptions and Discussion

The following are the simplifying assumptions:

1. The flow processes throughout the impeller are considered isentropic (a displacement thickness allowance for boundary layer growth may be made, however).
2. The flow is assumed axially symmetric and the mean flow path is assumed parallel to the blade mean lines.
3. The continuous flow variations in the impeller are presumed to be adequately represented by incremental changes along the radius r and the axis z . (See list of symbols in the appendix.)

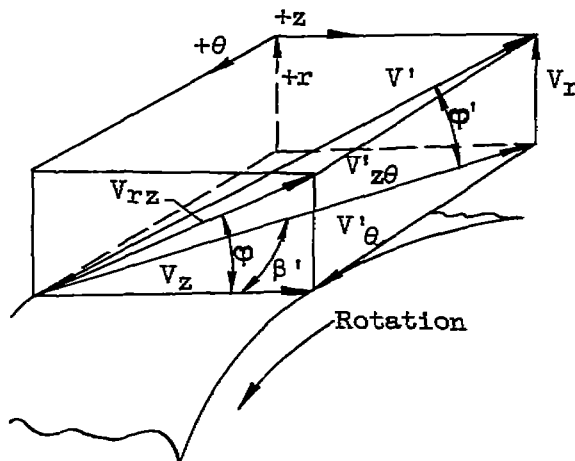
That the entire flow will not be isentropic is apparent. If, however, the pressure gradients can be maintained below the limit which will cause separation and boundary layer displacement thickness allowances are made thereby preventing choking and distorting of local stream tubes, the free-stream flow paths should not differ essentially from those isentropically computed. In the absence of large adverse pressure gradients the methods of reference 7 might be conveniently utilized to calculate the approximate boundary layer growth along any surface where the free-stream conditions are known.

The commonly used assumption of axial symmetry is strictly true only for an infinite number of zero thickness blades. This condition is

believed to be reasonably approximated for high solidity thin blades such as those of the present investigation (see ref. 8). Care should be exercised, however, and possibly special allowances made in the continuity equation when the blade mean relative Mach number approaches 1. Under these conditions the use of a sonic mean velocity in the continuity equation will overestimate the flow capacity of a passage with mean velocity in the transonic range.

Derivation of Equations

Nomenclature and coordinate system. - Throughout the current procedure cylindrical coordinates were used with the nomenclature illustrated in the following sketch. The relations between the various velocity components were developed as follows:



$$\cos \beta' = V_z / V'_{z\theta} \quad (1)$$

$$\sin \varphi' = V_r / V' \quad (2)$$

$$\tan \varphi = V_r / V_z \quad (3)$$

$$(V')^2 = (V'_{z\theta})^2 + (V_r)^2 \quad (4)$$

From equations (1) and (4),

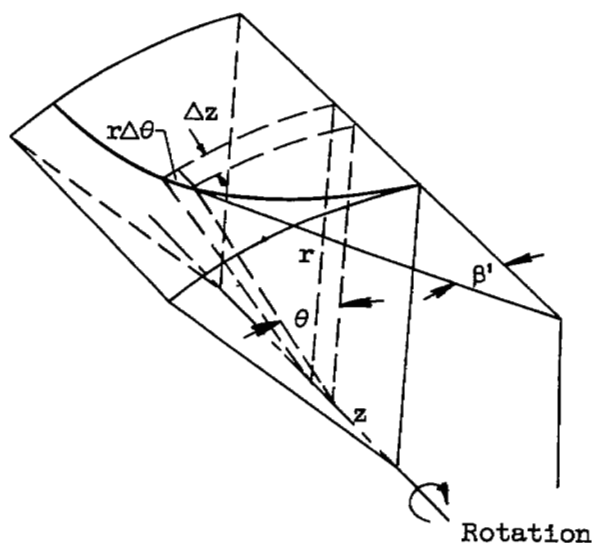
$$(V')^2 = \left(\frac{V_z}{\cos \beta'} \right)^2 + V_r^2 \quad (5)$$

From expressions (5) and (3),

$$V_z^2 = \frac{(V' \cos \beta')^2}{1 + \tan^2 \phi \cos^2 \beta'} \quad (6)$$

Determination of blade mean camber line. - Utilization of an analytical expression for the blade mean surface in three dimensions is convenient in the computations of the impeller flow. The following development with the aid of the sketch below relates the radius, axial position, and the angles β' and θ as required for radial blade elements:

$$\lim_{\Delta z \rightarrow 0} \frac{\Delta \theta}{\Delta z} = \frac{d\theta}{dz} = \frac{\tan \beta'}{r}$$



All linear dimensions may now be made dimensionless by dividing by the tip radius r_t . Then $d\theta/d(z/r_t)$ may be equated to a polynomial in z/r_t , such as in the following expression:

$$\frac{d\theta}{d(z/r_t)} = a \left(\frac{z}{r_t}\right)^2 + b \left(\frac{z}{r_t}\right) + c = \frac{\tan \beta'}{r/r_t} \quad (7)$$

In order to determine the coefficients a , b , and c , three conditions must be specified. The following three conditions are proposed for convenience:

1. At $z/r_t = 0$, $C = \tan \beta' / r/r_t$ where β' may be found as $\beta' = \tan^{-1} \omega r / V_{z,t}$ for no guide vanes. The value of V_z , which is the axial velocity component at the tip, is known from the inlet computations.

2. At $(z/r_t)_2$, β' may be specified at a particular radius, for example, $\beta'_2 = 0$.

3. The third condition may be selected so as to distribute the blade loading relatively uniformly over the blade surface. In the present design, a fixed angle corresponding to a predetermined degree of turning was specified for $z/r_t = 0.30$. In this manner, the peak loading was placed near the leading edge for the blade defined by the coefficients specified.

Blade thickness distribution. - A blade thickness distribution is specified along an initial streamline. For structural reasons a blade radial thickness taper with the maximum thickness at the hub is desirable. With the mean surface equation known, if a particular radial taper is set, the specification of the thickness distribution along one streamline fixes the entire blade geometry except for the unspecified radial boundaries.

Determination of pressure distribution around a blade element. - In order to evaluate the aerodynamic desirability of any given blade shape as determined by a mean line and a thickness distribution obtained from the preceding procedure, an estimate of the static-pressure or blade loading distribution is required. An approximate method for determining the static-pressure distribution follows. This procedure is a variation of that used in reference 9 utilizing moment of momentum principles. Though basically identical, the methods differ in two particulars. The current procedure involves the determination of blade surface velocities for a predetermined blade shape and the assumption of a linear variation of pressure between blade driving- and trailing-face surfaces. In reference 9 the blade loading diagrams were selected as desired and the blade shape was evolved from moment of momentum considerations; the velocity variations between blades were assumed linear.

The static-pressure difference across a blade passage in the tangential direction may be approximated by equating the rotor torque to the rate of change of angular momentum of the fluid. Then for constant radius,

$$\text{torque} = \text{Mass} \cdot r \cdot \Delta V_\theta$$

where ΔV_θ is the change in the absolute tangential velocity over the surface interval along the streamline for which the torque is computed.

Now

$$\int_{s_{n-1}}^{s_n} \Delta p_\theta \times r \times h \times dz = \frac{2\pi r_1}{N} h_1 \rho_1 V_1 \cos \beta_1 \cos \phi_1 \Delta V_\theta \times r \quad (8)$$

where ΔV_θ is the change in V_θ between stations $n-1$ and n in the radial-axial plane and this increment is selected sufficiently small that r may be considered constant, and Δp_θ is the net pressure acting in the tangential direction on the blade surface of height h between the stations $n-1$ and n .

In order to compute Δp_θ at any point z , the expression (8) may be written in the finite difference form below assuming a linear variation in the quantities for small differences $\Delta \frac{z}{r_t}$. The linear dimensions are made dimensionless through division by the tip radius r_t and ωr is in feet per second.

$$\left. \overline{\Delta p_\theta} \right|_{n-1}^n = \frac{\frac{2\pi}{N} \left(\frac{\bar{r}_1}{\bar{r}_t} \right) \cos \bar{\beta}_1' \bar{\rho}_1 \bar{V}_1' \cos \bar{\phi}_1'}{\left(\frac{\bar{r}}{\bar{r}_t} \right) \left(\frac{\bar{h}}{\bar{h}_1} \right) \Delta \frac{z}{\bar{r}_t} \Big|_{n-1}^n} \left[\left(\frac{\bar{r}}{\bar{r}_t} \right)_n (\bar{V}_{z\theta} \sin \bar{\beta}' - \omega \bar{r})_n - \left(\frac{\bar{r}}{\bar{r}_t} \right)_{n-1} (\bar{V}_{z\theta} \sin \bar{\beta}' - \omega \bar{r})_{n-1} \right] \quad (9)$$

This expression may be used within the accuracy of the current assumptions by utilizing the radial average of the upper and lower stream surface conditions along the mean radial position of the incremental annular segment. As a consequence of the assumption of axial symmetry, stream conditions are further averaged between the blade driving- and trailing-face values. In the above expression a single bar refers to the average or mean value between the appropriate boundaries, radial or tangential, and a double bar refers to conditions averaged in both directions.

The problem of obtaining the exact loading from the pressure difference Δp_θ has not yet been adequately solved. There are several assumptions, however, by which solutions may be obtained. For the current design a linear variation of pressure from blade driving to trailing face is assumed. The following expressions result for surface pressures:

$$p_{df} = \bar{p} + \Delta p_\theta / 2$$

$$P_{tf} = \bar{p} - \Delta p_\theta / 2$$

The blade driving- and trailing-face relative velocities may be readily obtained from the preceding surface static pressures in a manner which will be described later.

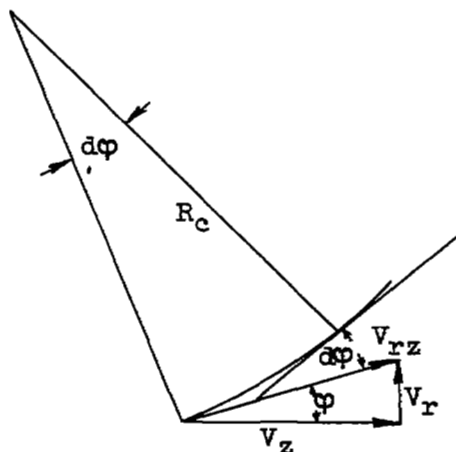
Determination of radial pressure gradient. - Within the assumption of axially symmetric, nonviscous flow the radial forces acting on the fluid particles passing through an impeller of the type where radial velocity components are relatively small may be approximated as shown below.

In references 10 and 11 (pp. 990-997) the radial component of Lorenz's equation of motion is given as

$$F_r = \frac{1}{\rho} \frac{\partial p}{\partial r} + \frac{d^2 r}{dt^2} - \frac{(\omega r + V_\theta')^2}{r}$$

However, for radial blades $F_r = 0$ and $\frac{1}{\rho} \frac{\partial p}{\partial r} = \frac{(\omega r + V_\theta')^2}{r} - \frac{d^2 r}{dt^2}$.

$$\frac{d^2 r}{dt^2} = \frac{d(V_r)}{dt} = \frac{d(V_{rz} \sin \varphi)}{dt} = V_{rz} \cos \varphi \frac{d\varphi}{dt} + \sin \varphi \frac{dV_{rz}}{dt}$$



From the preceding sketch, which shows the projection of a streamline in the radial-axial plane, $d\varphi = \frac{V_{rz} dt}{R_c}$ or $\frac{d\varphi}{dt} = \frac{V_{rz}}{R_c}$. In addition, $V_{rz} = \frac{ds}{dt}$ or $dt = \frac{ds}{V_{rz}}$, where 's' is the distance along a streamline projection in the radial-axial plane.

Now

$$\frac{1}{\rho} \frac{\partial p}{\partial r} = \frac{(\omega r + V_{\theta}')^2}{r} - \left(V_{rz} \cos \varphi \frac{d\varphi}{dt} + \sin \varphi \frac{dV_{rz}}{dt} \right)$$

or

$$\frac{1}{\rho} \frac{\partial p}{\partial r} = \frac{(\omega r + V_{\theta}')^2}{r} - \frac{V_{rz}^2}{R_c} \cos \varphi - V_{rz} \frac{dV_{rz}}{ds} \sin \varphi$$

Making all lengths dimensionless gives

$$\frac{1}{\rho} \frac{\partial p}{\partial \left(\frac{r}{r_t} \right)} = \frac{(\omega r + V_{\theta}')^2}{\frac{r}{r_t}} - \frac{V_{rz}^2}{\frac{R_c}{r_t}} \cos \varphi - V_{rz} \frac{dV_{rz}}{d \left(\frac{s}{r_t} \right)} \sin \varphi \quad (10)$$

The expression for radius of curvature of a smooth curve is used to evaluate R_c , the streamline radius of curvature in the radial-axial plane.

$$R_c = \frac{\left[1 + \left(\frac{dr}{dz} \right)^2 \right]^{3/2}}{\frac{d^2 r}{dz^2}} \quad (11)$$

In order to utilize equations (10) and (11) for obtaining the radial pressure gradients, reference is made to the third assumption that continuous variations are assumed to be adequately approximated by small finite incremental changes. Thus $dr/dz = \tan \varphi$ and

$d^2 r/dz^2 \approx \frac{\tan \varphi_n - \tan \varphi_{n-1}}{\Delta z}$, where subscripts $n-1$ and n are successive points along the streamline $\psi = \text{constant}$. R_c will have the sign $d^2 r/dz^2$ and will become the dimensionless term R_c/r_t when Δz is made dimensionless through division by r_t in the expression $d^2 r/dz^2$. Again considering the change along $\psi = \text{constant}$ from $n-1$ to n ,

$$\frac{dV_{rz}}{d \left(\frac{s}{r_t} \right)} \approx \frac{\Delta V_{rz}}{\Delta \left(\frac{s}{r_t} \right)} = \frac{(V_{rz})_n - (V_{rz})_{n-1}}{\left(\frac{s}{r_t} \right)_n - \left(\frac{s}{r_t} \right)_{n-1}}$$

where s/r_t is the dimensionless distance along the stream surface projection in the radial-axial plane.

Computation of radial boundary from continuity. - The continuity relation to be satisfied everywhere between the stream surfaces is

$$w_1 = \rho_1 \bar{V}_1 \cos \varphi_1 \times \frac{2\pi r_1}{N} h_1 = \rho \bar{V}' \cos \varphi' \cos \beta' \left(\frac{2\pi r}{N} - \frac{\tau}{\cos \beta'} \right) h$$

from which

$$\frac{h}{h_1} = \frac{\rho_1 \bar{V}_1 \cos \varphi_1 \frac{2\pi \frac{r_1}{r_t}}{N}}{\rho \bar{V}' \cos \varphi' \cos \beta' \left(\frac{2\pi \frac{r}{r_t}}{N} - \frac{\tau}{r_t \cos \beta'} \right)} \quad (12)$$

where subscript (1) refers to the rotor inlet and the double bar indicates the mean tangential and radial positions. The linear dimensions are made dimensionless on division by radius r_t . Other terms are defined in the list of symbols. The angles are approximated as follows:

$$\varphi = \tan^{-1} \left[\frac{\left(\frac{r}{r_t} \right)_{n+1} - \left(\frac{r}{r_t} \right)_n}{\left(\frac{z}{r_t} \right)_{n+1} - \left(\frac{z}{r_t} \right)_n} \right]$$

$$\varphi' = \tan^{-1} \left\{ \frac{\left[\left(\frac{r}{r_t} \right)_{n+1} - \left(\frac{r}{r_t} \right)_n \right]}{\left[\left(\frac{z}{r_t} \right)_{n+1} - \left(\frac{z}{r_t} \right)_n \right]} \cos \beta' \right\}$$

A convenient form of the energy equation as developed in reference (12) is given and may be used for computations of the stream density:

$$\frac{\rho}{\rho_{T,0}} = \left\{ \frac{\gamma-1}{2} \left[\left(\frac{\bar{\omega}_r}{C_{T,0}} \right)^2 - \left(\frac{\bar{V}'}{C_{T,0}} \right)^2 \right] + 1 \right\}^{\frac{1}{\gamma-1}} \quad (13)$$

where $C_{T,0}$ is the stagnation velocity of sound in front of the impeller.

Determination of velocities from energy relations. - In order to obtain the mean velocity distribution on a new streamline from the known velocities on an adjacent streamline and the known Δp_r distribution

between the streamlines, the energy equation and the adiabatic relation may be utilized. The energy equation is given in a convenient form for

$$\left[\frac{(\bar{\bar{V}}'_{m+1})^2}{2} + C_p t_{m+1} \right] - \left[\frac{(\bar{\bar{V}}'_m)^2}{2} + C_p t_m \right] = \frac{(\omega r_{m+1})^2 - (\omega r_m)^2}{2}$$

or

$$(\bar{\bar{V}}'_{m+1})^2 = (\omega r_{m+1})^2 - (\omega r_m)^2 + 2C_p (t_m - t_{m+1}) + (\bar{\bar{V}}'_m)^2$$

where the subscripts m and $m+1$ refer to the adjacent streamlines $\psi = m$ and $\psi = m+1$. The double bar indicates the mean radial position and the mean tangential position between the driving and trailing faces.

$$\text{If } t_m - t_{m+1} = (\Delta t)_r,$$

$$(\bar{\bar{V}}'_{m+1})^2 = (\omega r_{m+1})^2 - (\omega r_m)^2 + 2C_p (\Delta t)_r + (\bar{\bar{V}}'_m)^2 \quad (14)$$

For the case where the computations proceed inward toward the axis, $(\Delta t) = t_{\text{upper mean line}} - t_{\text{lower mean line}}$. If the flow is considered isentropic the temperature at $m+1$ may be found from $(\Delta p)_r$ using the adiabatic expression

$$t_{m+1} = t_m \left(\frac{p_{m+1}}{p_m} \right)^{\frac{\gamma-1}{\gamma}} = \left(\frac{p_m - \Delta p_r}{p_m} \right)^{\frac{\gamma-1}{\gamma}} \times t_m$$

or

$$\Delta t_r = t_m \left[1 - \left(1 - \frac{\Delta p_r}{p_m} \right)^{\frac{\gamma-1}{\gamma}} \right] \quad (15)$$

The right side of this equation may be replaced by the first three terms of a binomial series expansion with essentially no error.

General computational procedure. - After a satisfactory blade mean line and thickness distribution have been established, the hub and tip contours required to pass the desired weight flow and satisfy the conditions prescribed along the initially specified streamline must be obtained. The proposed procedure may be considered as a stream filament method applied through the inlet section and the impeller. The flow at the entrance to the inlet section is first divided into several segments

of radial height h_0 . With the specified streamline as one boundary, the variation in h for the adjacent stream tube through the entrance section and rotor (along z) necessary to satisfy continuity is obtained from equation (12). The radial gradient in pressure and the velocity on the subsequent streamline are next computed from the flow on the specified streamline with the aid of equations (10) and (14). The pressures along the adjacent streamline are estimated by extrapolating the pressure gradients over the distances h obtained from continuity. A more accurate estimate of the mean annular conditions may now be obtained from the values on the upper and lower boundaries. These mean conditions may now be used to obtain the final orientation of and the conditions along the second streamline. This process may be continued progressing from the specified streamline in either or both radial directions until the desired mass flow is contained.

The blade loading may be estimated from expression (9) derived from moment of momentum considerations.

Application of Equations to Compressor Design

The expressions previously derived or presented may be utilized in the detailed computation of the inlet and impeller configuration in the following manner.

Entrance section. - The entrance conditions may be computed by means of the same relations utilized in the rotor. The rotor equations reduced to the absolute reference frame for use in the inlet are as follows:

From continuity

$$\frac{h}{h_0} = \frac{\rho_0 v_0 \left(\frac{r}{r_t} \right)_0}{\rho v \left(\frac{r}{r_t} \right) \cos \varphi}$$

where

$$\rho = \left[\frac{\rho_{T,0}}{\rho_0} \left(\frac{P_0}{P_{T,0}} - \frac{\gamma-1}{\gamma} \frac{v^2}{2} \right) \right]^{\frac{1}{\gamma-1}}$$

Upon elimination of blade considerations the radial pressure gradient becomes

CONFIDENTIAL

$$\frac{1}{\rho} \frac{\partial p}{\partial \left(\frac{r}{r_t} \right)} = - \frac{V_{rz}^2 \cos \varphi}{\frac{R_c}{r_t}} - V_{rz} \frac{dV_{rz}}{d \left(\frac{s}{r_t} \right)} \sin \varphi$$

The energy equation yields Mach number and hence velocity directly in the following form:

$$M = \left\{ \frac{2}{\gamma-1} \left[\left(\frac{P_0}{P} \right)^{\frac{\gamma-1}{\gamma}} - 1 \right] \right\}^{1/2}$$

In a manner identical to that described under the general procedure, the velocities may be specified on a single streamline in the entrance region starting from some position upstream of the impeller and ending at the impeller blade leading edge. By computing the streamlines radially away from the one specified, as was described for the impeller, the inner and outer walls upstream of the impeller may be computed.

Matching of entrance and blade leading-edge conditions. - If the rotor blades are restricted to radial elements, as is done in equation (7), the blade angle will match the inlet flow angle at a constant axial position ($z = 0$) at all radii only for the case of a constant entrance velocity with no prewhirl.

If an inflow velocity other than constant is desired at the leading edge of a blade with radial elements, a swept leading edge is required to match the inflow and blade angles at all radii. The following semi-graphical procedure may be utilized in obtaining the blade leading-edge contour:

In the region near the leading edge, the relative flow angle, obtained from the rotational velocity and the velocity determined from the solution of the inlet flow along the streamline, is computed for several stations along z . From the values of r/r_t obtained for the streamline in the inlet section, the corresponding blade angle is computed, using the prescribed equation for the blade mean surface. The z -position at which the relative inflow angle matches the blade angle establishes the blade leading edge for zero incidence angle.

Blade leading-edge thickness. - The leading-edge thickness may be specified arbitrarily or from structural requirements. Usually, in order to minimize the leading-edge disturbance, the smallest practical leading-edge angle and thickness are utilized. The leading-edge angle

may, in general, be defined as $2 \tan^{-1} \frac{\tau}{\Delta z / r_t}$ where τ is the blade thickness on the subject streamline and is located $\Delta(z/r_t)$ behind the

2714

blade leading edge. At this point τ may be determined from the radial thickness taper and the blade thickness at the corresponding z -position on the previous streamline.

When this procedure is applied to compressors having subsonic or transonic relative inlet velocities some deviation from smooth inlet flow is probably unavoidable, with the magnitude of the disturbance a function of the perturbations caused by the blades. For supersonic blades, however, the disturbances may, if desired, be contained within the blades by suitable selection of the number of blades and their thickness.

COMPUTATIONAL EXAMPLE AND DESIGN RESULTS

In order to illustrate the order of the computational procedure, the following abbreviated example of the process followed in the design of the subject impeller is presented along with the design results.

The following constants were initially specified:

$$D_t = 12.00 \text{ in.}$$

$$U_t = 1200 \text{ ft/sec}$$

$$\beta'_2 = 0 \text{ for all radii}$$

$$D_H/D_t = 0.40 \text{ at the inlet}$$

$$\text{Axial depth} = 6.00 \text{ in. at the hub}$$

$$M_t = 0.97 \text{ at the inlet}$$

Blade mean line specification. - A cylindrical outer shroud was selected and the initial streamline was specified on this surface. The blade mean surface, which under the assumption of axial symmetry is identical with the mean relative stream surface, is obtained from equation (8) where the constant coefficients are fixed by the following conditions on the tip streamline.

$$1. \beta'_1 = \tan^{-1} \omega r_t / V_z$$

$$2. \beta'_2 = 0$$

$$3. \beta' (z/r_t = 0.30) = 35^\circ$$

The blade mean surface is thus represented by the equation

$$2.354 (z/r_t)^2 - 4.060 z/r_t + 1.706 = \tan \beta' / r/r_t$$

Specification of blade thickness. - The blade thickness distribution about the tip mean line previously defined was arbitrarily fixed at the minimum values believed to be structurally sound. The blade thickness measured normal to the blade mean line is given in figure 1.

The thickness taper was defined by a blade included angle of 1° between the driving and trailing face blade elements in the plane normal to the blade mean line at that point. The blade thickness at any radius is then obtained from the corresponding blade tip thickness as

$$\tau/r_t = (\tau/r_t)_t + [(r/r_t)_t - (r/r_t)] 0.01714$$

No allowance for boundary layer was made in these calculations. However, a displacement thickness allowance may be conveniently applied to either the thickness distribution or the computed value of h if desired.

Computation of radial boundaries. - Equations (11) and (12) were utilized to compute the annular segmental boundaries progressively from the tip cylindrical boundary to the hub contour. The resulting hub contour gave a hub radius ratio change from 0.40 at the inlet to 0.619 at the exit. Equations (13), (14), (15), and (16) were used to obtain the radial pressure gradients and velocity as these quantities are necessary to the boundary computations.

Determination of blade sweepback. - In the process of computing the radial boundaries, the location of the impeller blade leading edge is accomplished in the manner previously described by matching the blade mean surface to the inlet relative flow direction. The total blade leading-edge sweepback of the subject impeller is found to be

$$(z/r_t)_t - (z/r_t)_H = 0.197$$

Computation of blade loading characteristics. - The radial average of the blade loading in an annular segment of height h may be estimated from a solution of equation (10). The tip loading in terms of the driving and trailing face velocities is plotted in figure 2.

Design performance. - The design resulted in the following theoretical performance:

Over-all pressure ratio of impeller less normal shock losses = 2.41.

Maximum design speed weight flow = 30.8 lb/sec (39.2 lb/sec-sq ft of frontal area).

Over-all adiabatic efficiency considering only normal shock losses = 0.852.

2714

The tip inlet velocity diagram is shown in figure 3, while figure 2 gives the comparable loading diagram and mean velocity distribution. The restriction to a small rise in mean velocity through the impeller was intended to reduce the amount of deceleration on the blade trailing face at the critical trailing-edge portion. In spite of this unorthodox mean pressure decrease through the impeller, the trailing-face velocity (fig. 2) still undergoes a substantial deceleration as the flow approaches the trailing edge. The effects of this deceleration on wake thickness and separation tendencies are not known.

Actually only the loading trends can be obtained from the moment of momentum; thus, it does not appear likely that the blade would unload before the trailing edge as indicated in figure 2. This phenomenon results from an inflection point in the blade mean line to which the relative rotor flow is assumed parallel.

EXPERIMENTAL APPARATUS AND TEST PROCEDURE

The transonic impeller which was machined from a solid 14S-T aluminum forging is pictured in figure 4. It was tested in the 3000 horsepower rig shown schematically in figure 5. The piping provided for refrigerated or atmospheric inlet air as well as altitude exhaust. A calibrated submerged adjustable orifice was used to measure the weight flow. Most of the tests were run at 15 inches of mercury absolute inlet pressure. No differentiation is made between these tests and those few made with atmospheric inlet pressure, since no distinct differences could be observed in the reduced data.

The instrumentation consisted of temperature and pressure probes (fig. 5) plus static-pressure orifices located along the outer casing before, over, and after the impeller. Static-pressure orifices were also located along the inner wall (hub) before and after the impeller. Five calibrated double stagnation thermocouple probes were located 6 inches downstream of the impeller trailing edge. The annulus area was divided into five equal annular rings and a probe located in the center of each ring. Six spike-type thermocouples, six total-pressure, and two static-pressure probes were located in the inlet depression tank where the total area was such that the static and total pressures were essentially equal.

A probe actuator was located downstream of the impeller as indicated in figure 5 so that either a combination cone probe (static and total pressure plus yaw) or a claw total-pressure probe could be used approximately 1 inch behind the impeller blade trailing edge.

0

Both probes were calibrated for angle in a subsonic and supersonic stream. The cone probe was calibrated for angle and static pressure. For Mach numbers above approximately 1.05, a close agreement was noted between the computed surface static pressure and that measured on the surface of the cone. When the claw total probe was used, the stream static pressure was obtained by interpolation between the inner and outer wall orifice measurements. Ten survey points were usually taken across the approximately 2 inch impeller exit annulus.

Accuracy of data. - Observed measurements are estimated to be accurate within the following limits:

Temperature, °F	±0.8
Pressure, in. Hg	±0.05
Air weight flow, percent	±1.0
Impeller speed, percent	±0.5

On the basis of these tolerances, the maximum errors in the performance figures are approximately

Pressure ratio (at lowest value)	0.008
Adiabatic efficiency (percent at lowest temperature rise) . . .	2.5

No tolerances are given for the angular measurements inasmuch as they have small effect on the total-pressure ratio and adiabatic efficiency and moreover are difficult to estimate with any degree of assurance in the impeller wakes.

In the table of performance data (table I) two adiabatic efficiency points at a tip speed of 500 feet per second have values equal to or slightly exceeding 1.00 (1.00 and 1.03). The combination of temperature and pressure errors giving the maximum adiabatic efficiency error would reduce the recorded efficiency only 2.5 percent. There is one other source of error, however, which is not exactly a function of the accuracy of measurements. During the testing period the necessity of holding conditions constant for a considerable period was found necessary in order to obtain stable temperature readings. This phenomenon has been commonly noted where there is high heat capacity. Hence the theory is advanced that those efficiency points exceeding 1.00 have an additional small error because of insufficient time allowance for the measured temperature to reach its maximum value for the fixed conditions.

Within the limitations specified, the data provided by this instrumentation were reduced to the performance data presented.

EXPERIMENTAL RESULTS AND DISCUSSION

Over-all Performance

271. Presentation of the 12-inch transonic mixed-flow impeller performance characteristics is complicated by a data deficit resulting from inability to obtain the high weight flow side of the performance map. Because of these conditions care was exercised in an attempt to eliminate erroneous conclusions which might result from the inadequate data. The measured over-all performance is given in table I and in figure 6 which shows adiabatic efficiency contours superimposed on a plot of impeller pressure ratio against equivalent weight flow for 500, 700, 800, 1000, 1100, and 1200 feet per second equivalent tip speeds. It is apparent that only the low weight flow portion of the curve is shown in figure 6. The shape of the curves indicates that the peak impeller pressure ratio was not attained. That part of the performance map determined at all speeds above 800 feet per second was considerably below design expectations. There are several indications, which will be discussed later, that choking in the annulus after the impeller is responsible for the failure to obtain the weight flow corresponding to peak pressure ratio.

Observation of the pressure ratio weight flow curves (fig. 6) shows that only the lowest tip speed (500 ft/sec) indicates pressure ratio and efficiency peaks at less than the maximum measured flow; all other curves display continually rising pressure ratio and efficiency with weight flow up to a maximum. Moreover, there is a relatively small increase in weight flow with speed which is reflected in the large increase in minimum angle of incidence with speed shown in figure 7. It might be expected that, for minimum back pressure on the rotor, the axial inlet velocity (hence, weight flow) would increase with speed to an extent at least sufficient to maintain nearly constant impeller blade incidence angle. This characteristic, which should be exhibited even by a choked impeller, is not apparent. Instead, the incidence angle (fig. 7) increases with speed. This condition is clearly not characteristic of an unrestricted flow path.

Impeller Flow Limits

Impeller inlet flow. - Utilizing the current design procedure, the resulting transonic impeller blade leading edges were swept behind the hypothetical Mach cone based on the theoretical relative inlet Mach number. The structural and aerodynamic effects of this configuration were considered desirable. Although the inability of such a leading edge to support an attached shock is well known, the significance of its effect on impeller flow inducement is not yet fully recognized. Deviation from the conventional theoretical supersonic compressor inlet phenomena (ref. 3) appears more a difference of degree than character, since the

CONFIDENTIAL

existence of subsonic axial-flow velocities before any type impeller precludes the exclusive existence on the blade trailing face of either compressions or expansions without subsequent waves of the opposite sign. In any case, however, the blade trailing-surface contour is probably still a contributing factor in the determination of the inflow velocity. One characteristic difference between the swept and unswept blade lies in the ability of the hub inlet flow to effect the rotor inlet flow at larger radii. No comprehensive experimental evaluation of the swept blade effects can be gathered from the current work because of the aforementioned flow restriction, which prevented the attainment of design inlet conditions.

Flow limits. - A reasonably regular curve could be drawn through the maximum weight flow points of figure 6. The minimum measured weight flow points, however, do not allow a regular curve at all. The reason for this must be found in the inability to locate a surge point at any speed. Moreover, continual cognizance of the threat of structural failure along with observation of the vibrations with increased back pressure prevented more elaborate exploration in the low weight flow regions. Only for the run at 1100 feet per second, where there was unusually smooth operation, is there any indication of a flow limit. The static-pressure distribution along the outer casing is shown in figure 8 for maximum and minimum weight flow points at tip speeds of 500, 1100, and 1200 feet per second. For the upper curve at 1100 feet per second which corresponds to a much lower flow than the minimum 1200 feet per second flow point, the ratio of the local static pressure to the inlet total pressure may be seen to be of the order of unity at the impeller tip leading edge indicating a generally stagnant region, although there was no indication of audible surge. The type of stall, whether rotating or stationary, and its radial extent were not known. Because it was observed that any back pressure change which changed the outlet conditions is immediately felt upstream even near maximum flow, the impeller itself is clearly unchoked.

The original test program for the transonic mixed-flow impeller was to include a complete stator investigation following the impeller tests. These plans were altered when design impeller performance could not be obtained. It was thought, however, that perhaps the installation of stators would make possible an improvement in impeller performance by turning the outlet flow in a direction which would increase the effective flow area, thereby helping to remove the choked region in the exit annulus. Thus stators were designed and built for a combination of the theoretical and experimental rotor exit flow conditions. As indicated by the tailed symbols in figure 6, only scant reduction in the flow restriction was noted. This amount of improvement was felt to be distinct but insufficient to justify a detailed stator program; hence no further reference will be made to the stators, which basically had the effect of a small reduction in back pressure on the impeller.

Comparison of design and experimental performance. - The inability to obtain design weight flow makes it impossible to determine conclusively whether the design procedure accurately predicts the experimental flow. No detailed analysis was made by which the exact angle of incidence could be determined. The design computations were made for conditions which would be compatible with essentially zero angle of incidence at design flow.

For the current design the mean static-pressure distribution along a streamline $\psi = \text{constant}$ varied from nearly constant at the tip to a rapidly falling static pressure along the hub boundary. Thus the energy addition at design speed would be added all in the form of kinetic energy if design flow was realized. This condition, which should lead to efficient rotor flow, may lead to severe stator starting problems because of the high Mach number and consequently high shock loss level (see, e.g., ref. 13). Moreover, when these starting difficulties exist, even the advantage of a favorable mean gradient in the impeller is questionable. Therefore, inasmuch as the axial-flow transonic work of reference 6 has indicated that a moderate static-pressure increase still gives very high efficiencies in the transonic speed range, the use of an increasing mean static pressure everywhere through the impeller would provide better over-all performance.

Reference to the incidence angles (table I) indicates that the measured values do not approach the design values (approximately zero) as the design speed is approached. Instead, the angles increase, indicating that the flow restriction becomes more severe with increasing speed, possibly because of the increasing boundary layer growth and losses through the impeller which allowed scant increase in weight flow for the increase in rotor output.

Table I also indicates that $M_{1,H}$ is equal to or greater than $M_{1,t}$ at each minimum weight flow point except that for a tip speed of 1200 feet per second, where data were obtained for only a small weight flow range. While it does not appear feasible to detail the procedure by which the rotor flow breaks down, the deterioration of the tip flow clearly precedes that of the hub, a phenomenon associated more closely with the stall or surge region than design operation, however.

As shown in figure 9, the variation in both the theoretical and experimental total-pressure ratios over the outlet annulus is large. This variation is probably detrimental from both the viewpoint of difficulty of staging and efficiency of stator diffusion since the radial energy gradient would probably lead to excessive mixing in the diffusing process after the dynamic balance is relaxed. For this particular impeller, which was designed to investigate other aspects of impeller performance, the radial variation in total pressure was not considered

CONFIDENTIAL

important. However, the required alteration to the design procedure could be made to maintain constant theoretical work input along the radius, particularly if the restriction to radial blade elements is eliminated or relaxed. The total-pressure ratio or work output variation would then be a function of the efficiency variation along the blade span.

Blade Structural Failure

During a routine inspection after approximately 35 hours and 15 minutes running time, one of the impeller blades was found to have a $1\frac{1}{2}$ inch crack beginning at the leading edge and running just above and nearly parallel to the hub. The crack closely checked a nodal point located as shown by the inner sand pattern (fig. 4) during a preliminary check of the static vibrational characteristics of the impeller. The frequency of this mode of static vibration was observed to be between 1180 and 1210 cycles per second. A small amount of undercut had previously been noted at the hub of each blade. This defect, coupled with the existence of several relatively easily excited vibrational modes, indicated the possibility of this type failure.

The impeller was cut from a solid aluminum forging and hence provided little internal damping. However, since the original crack plus a smaller one of the same type discovered later were small, it was felt that some further tests might be run if some form of damping could be installed. Consequently, a 0.030 inch hole was drilled in each blade in the tangential direction at a point midway between the hub and tip near the leading edge. Through the holes were strung 18 loops of 0.006 inch light filament wire. The two ends were cemented, one on each side of one of the blades (fig. 10). This arrangement reduced the previously recorded static natural frequencies to approximately one-seventh their previous values. With this configuration the originally scheduled test points were completed in about 6 hours running time before the wire failed, probably because of the unequal tension on the loops. Little, if any, further deterioration of the blades was observed and no apparent aerodynamic effects of the wire could be detected.

CONCLUDING REMARKS

An analytical and experimental study of a high solidity transonic impeller was made.

An approximate procedure for design of high solidity impellers assuming axially symmetric, nonviscous flow is developed and presented along with the design and experimental results for a 12-inch-diameter, swept back leading edge, transonic, axial discharge impeller.

2714

Test results at the design equivalent tip speed of 1200 feet per second indicated a maximum pressure ratio of only 2.164 at a weight flow of 26.47 pounds per second (33.71 lb/sec-sq ft) and an impeller adiabatic efficiency of 0.81. The measured performance was restricted particularly at and near design speed to performance figures considerably below theoretical by a flow restriction in the outlet annulus. The low speed performance appeared very good. Partial structural failure of the impeller occurred before alleviation of the outlet annulus flow restriction could be accomplished.

The effects of blade sweep back, though not fully understood, do not appear undesirable inasmuch as this impeller operated without audible surge in spite of very large incidence angles.

Test results and analysis strongly indicate that for future designs a rise in mean static pressure through the impeller in order to reduce absolute discharge velocity and an approach to equal energy input along the rotor blade span are desirable.

Lewis Flight Propulsion Laboratory
National Advisory Committee for Aeronautics
Cleveland, Ohio

APPENDIX - SYMBOLS

The following symbols are used in this report:

C	velocity of sound, ft/sec
C_p	specific heat at constant pressure, ft-lb/(slug)(°F)
D	impeller diameter, ft
d/dt	derivative with respect to time
F	force per unit mass
h	height of annular stream tube, ft
M	absolute Mach number, ratio of absolute air velocity to local velocity of sound
M'	relative Mach number, ratio of air velocity relative to rotor to local velocity of sound
m,1,2	streamline number
N	number of blades
P	total pressure, lb/sq ft
p	stream pressure, lb/sq ft
R_c	radius of curvature in radial-axial plane, ft
r	compressor radius, ft
s	streamline projection in radial-axial plane, ft
t	stream temperature, °R
U	velocity of rotor (ωr) at radius r, ft/sec
V	absolute velocity, ft/sec
V'	velocity relative to rotor, ft/sec
W	weight flow, lb/sec
w	weight flow between adjacent streamlines

CONFIDENTIAL

2710

α	incidence angle, angle between inlet flow and blade mean line at leading edge
β	angle between compressor axis and absolute flow direction, deg
β'	angle between compressor axis and air velocity relative to rotor, deg
γ	ratio of specific heats
δ	ratio of actual inlet total pressure to standard sea-level pressure $P_{T,0}/2116$
η_{ad}	adiabatic efficiency
θ	angle between blade element at blade leading edge and subsequent element both projected on plane perpendicular to compressor axis, radians (see sketch preceding eq. (1))
$\sqrt{\theta}$	square root of ratio of actual inlet stagnation temperature to standard sea-level temperature, $\sqrt{T_0/518.4}$
ρ	fluid density, slugs/cu ft
τ	blade thickness
φ	upsweep angle, $\tan^{-1} V_r/V_z$
φ'	$\tan^{-1} V_r/V_{z\theta}$
ψ	stream function along which $w = \text{constant}$
ω	angular velocity, radians/sec

Subscripts:

df	driving face of blade
H	hub
m	midpoint of a particular incremental annulus
n	points along a streamline
r	radial component
rz	radial-axial plane

CONFIDENTIAL

T	total
t	tip
tf	trailing face of blade
z	axial component
z θ	axial-tangential plane
θ	tangential component
O	position at beginning of entrance section
1	impeller inlet
2	impeller exit

REFERENCES

1. Bogdonoff, Seymour M.: N.A.C.A. Cascade Data for the Blade Design of High-Performance Axial-Flow Compressors. Jour. Aero. Sci., vol. 15, no. 2, Feb. 1948, pp. 89-95.
2. Kantrowitz, Arthur, and Donaldson, Coleman duP.: Preliminary Investigation of Supersonic Diffusers. NACA WR L-713, 1945. (Supersedes NACA ACR L5D20.)
3. Kantrowitz, Arthur: The Supersonic Axial-Flow Compressor. NACA Rept. 974, 1950. (Supersedes NACA ACR L6D02.)
4. Erwin, John R., Wright, Linwood C., and Kantrowitz, Arthur: Investigation of an Experimental Supersonic Axial-Flow Compressor. NACA RM L6J01b, 1946.
5. Johnsen, Irving A., Wright, Linwood C., and Hartman, Melvin J.: Performance of 24-Inch Supersonic Axial-Flow Compressor in Air. II - Performance of Compressor Rotor at Equivalent Tip Speeds from 800 to 1765 Feet Per Second. NACA RM E8G01, 1949.
6. Lieblein, Seymour, Lewis George W., Jr., and Sandercock, Donald M.: Experimental Investigation of an Axial-Flow Compressor Inlet Stage Operating at Transonic Relative Inlet Mach Numbers. I - Over-All Performance of Stage with Transonic Rotor and Subsonic Stators Up to Rotor Relative Inlet Mach Number of 1.1. NACA RM E52A24, 1952.
7. Tucker, Maurice: Approximate Turbulent Boundary-Layer Development in Plane Compressible Flow Along Thermally Insulated Surfaces with Application to Supersonic-Tunnel Contour Correction. NACA TN 2045, 1950.

- 2714
8. Wu, Chung-Hua, and Brown, Curtis A.: Method of Analysis for Compressible Flow Past Arbitrary Turbomachine Blades on General Surface of Revolution. NACA TN 2407, 1951.
 9. Stanitz, John D.: Approximate Design Method for High-Solidity Blade Elements in Compressors and Turbines. NACA TN 2408, 1951.
 10. Hamrick, Joseph T., Ginsburg, Ambrose, and Osborn, Walter M.: Method of Analysis for Compressible Flow Through Mixed-Flow Centrifugal Impellers of Arbitrary Design. NACA Rep. 1082, 1952. (Supersedes NACA TN 2165.)
 11. Stodola, A.: Steam and Gas Turbines. Vol II. McGraw-Hill Book Co., Inc., 1927. (Reprinted, Peter Smith (New York), 1945.)
 12. Stanitz, John D.: Two-Dimensional Compressible Flow in Turbo-machines with Conic Flow Surfaces. NACA Rep. 935, 1949. (Supersedes NACA TN 1744.)
 13. Klapproth, John F., Ullman, Guy N., and Tysl, Edward R.: Performance of an Impulse-Type Supersonic Compressor with Stators. NACA RM E52B22, 1952.

TABLE I. - PERFORMANCE DATA

Equivalent tip speed, $\frac{U_t}{\sqrt{\theta}}$	Pressure ratio, P_2/P_0	Adiabatic efficiency, η_{ad}	Equivalent weight flow, $\frac{W\sqrt{\theta}}{g}$	Tip angle of incidence, α_t	Hub angle of incidence, α_H	Absolute inlet Mach number at tip, $M_{1,t}$	Absolute inlet Mach number at hub, $M_{1,H}$
1198	2.16	0.81	26.47	19°32'	5°39'	0.54	0.49
1202	2.14	.79	26.04	19°30'	6°45'	.54	.47
1199	2.10	.77	25.19	21°54'	7°14'	.48	.46
1198	2.07	.76	24.27	23°10'	8°56'	.45	.44
1196	2.06	.76	23.42	24°12'	9°49'	.43	.42
1101	2.00	0.86	25.80	18°16'	4°31'	0.53	0.47
1099	1.87	.76	22.83	23°15'	8°57'	.41	.40
1100	1.79	.71	18.97	28°25'	15°02'	.31	.32
1099	1.70	.64	14.73	36°00'	13°44'	*.17	.33
958	1.79	0.93	24.85	15°55'	2°02'	0.503	0.44
1000	1.79	.84	24.36	17°53'	3°52'	.483	.43
998	1.68	.76	22.94	20°57'	6°40'	.42	.39
999	1.69	.75	21.39	23°41'	9°00'	.37	.36
998	1.63	.70	19.57	26°18'	11°15'	.32	.33
799	1.51	0.91	23.59	12°07'	-0°53'	0.49	0.41
799	1.48	.87	21.98	15°49'	1°59'	.42	.37
800	1.49	.88	20.93	16°01'	2°19'	.41	.37
799	1.45	.83	20.02	19°33'	5°13'	.36	.33
802	1.47	.85	18.91	18°44'	5°34'	.37	.33
799	1.43	.79	18.25	23°53'	7°55'	.29	.30
799	1.41	.77	16.37	25°32'	10°35'	.27	.27
700	1.39	0.95	22.09	10°50'	-1°33'	0.44	0.37
701	1.37	.90	20.20	14°45'	1°03'	.38	.33
700	1.35	.87	18.49	17°44'	3°23'	.34	.31
699	1.33	.81	16.65	21°38'	7°11'	.28	.27
699	1.31	.77	14.52	25°58'	11°32'	.23	.27
699	1.28	.70	12.40	28°47'	14°36'	.19	.21
500	1.19	0.95	20.36	3°28'	-7°37'	0.41	0.34
502	1.19	.96	19.72	4°56'	-6°43'	.39	.32
500	1.21	1.03	19.37	3°45'	-7°45'	.41	.34
500	1.18	.92	17.46	9°14'	-2°26'	.33	.27
499	1.19	.98	17.19	7°50'	-4°22'	.35	.29
500	1.19	.94	15.53	11°48'	-1°21'	.30	.26
500	1.20	1.00	15.43	13°34'	0°35'	.28	.24
500	1.18	.92	14.25	14°51'	1°40'	.27	.23
500	1.18	.88	13.21	19°18'	4°46'	.22	.21
500	1.14	.72	10.31	25°13'	9°53'	.17	.17

* Measured static pressure at this point exceeds upstream total pressure.
An orifice 1/2 inch upstream of the impeller inlet gave $M_{1,t} = 0.17$.



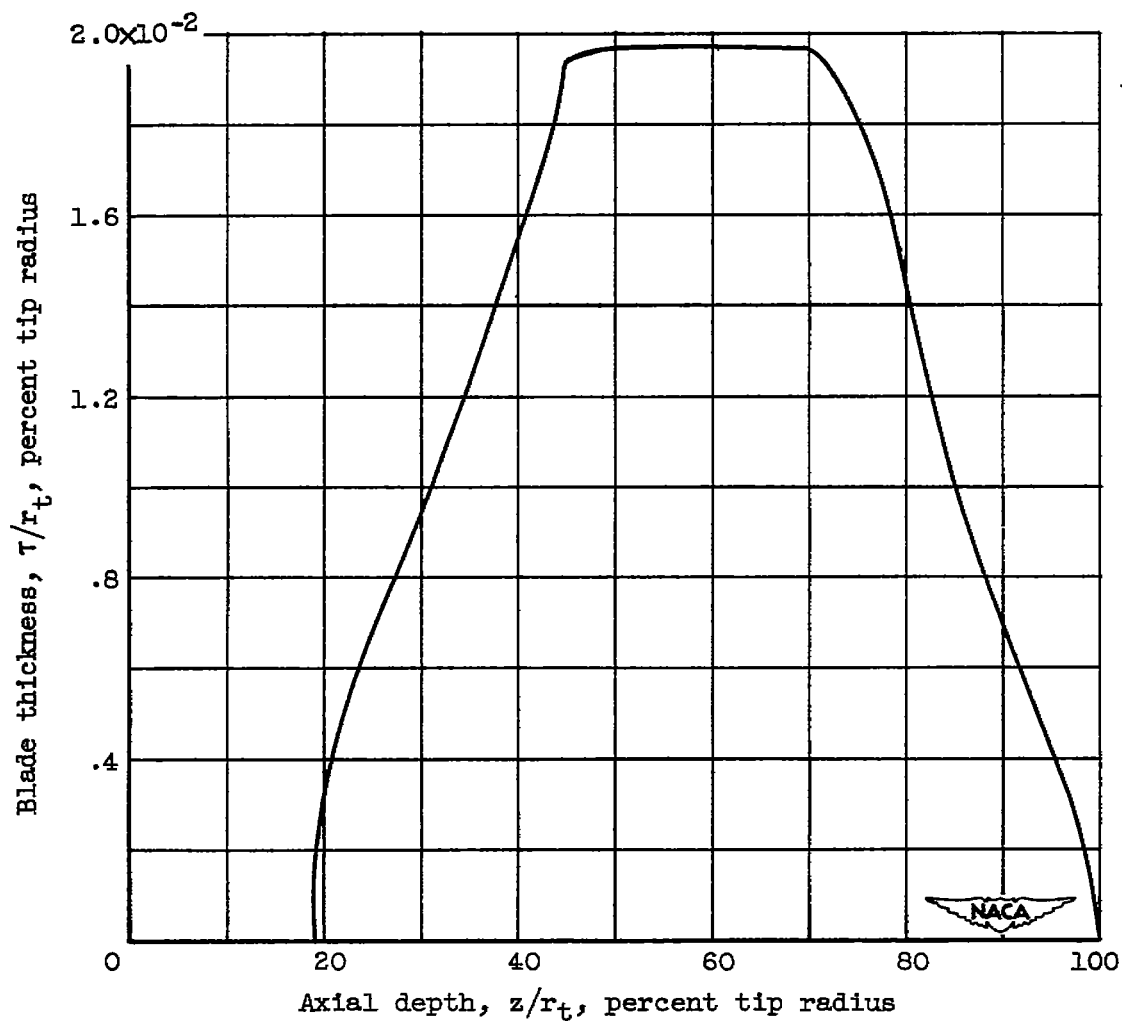


Figure 1. - Blade thickness distribution along tip mean line.

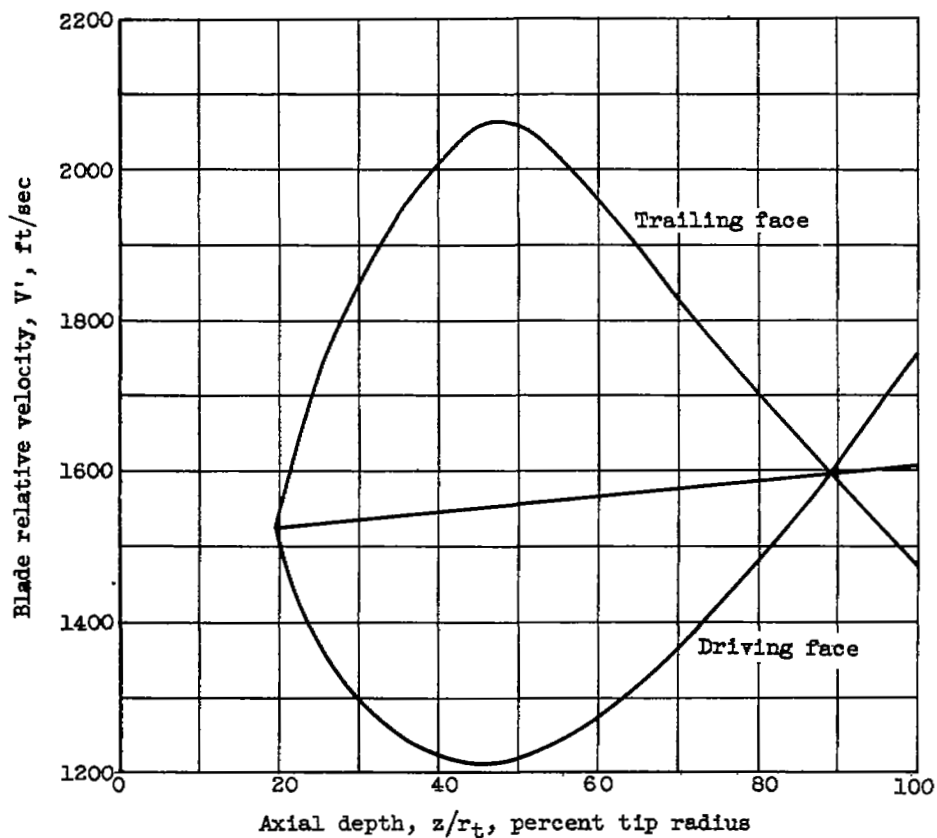


Figure 2. - Blade loading at tip radial station $r/r_t = 0.97$.

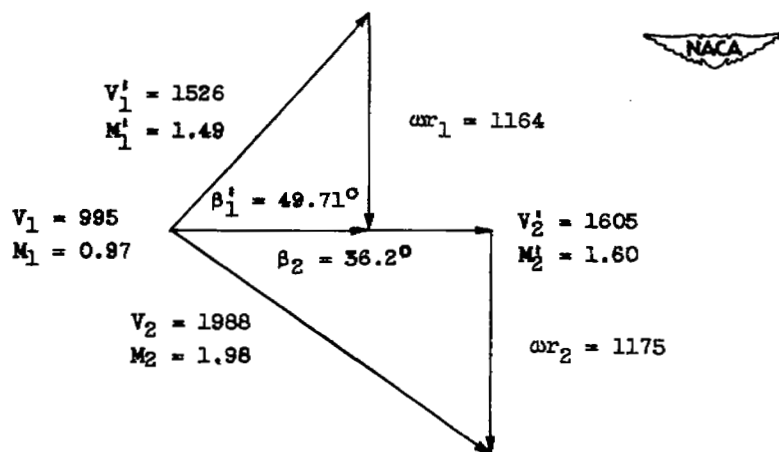


Figure 3. - Velocity diagram for tip mean annular streamline.

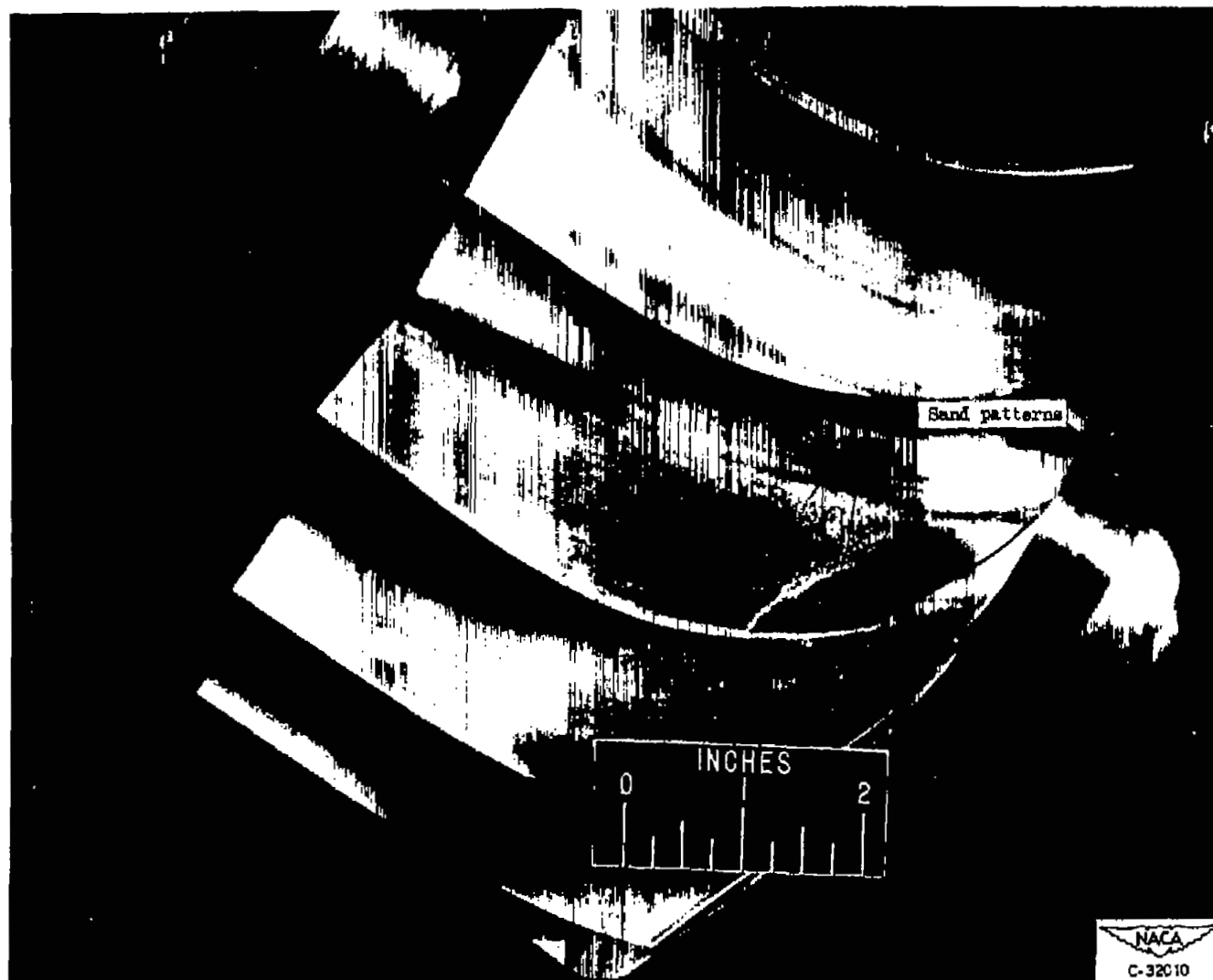


Figure 4. - 12-inch transonic high solidity impeller.

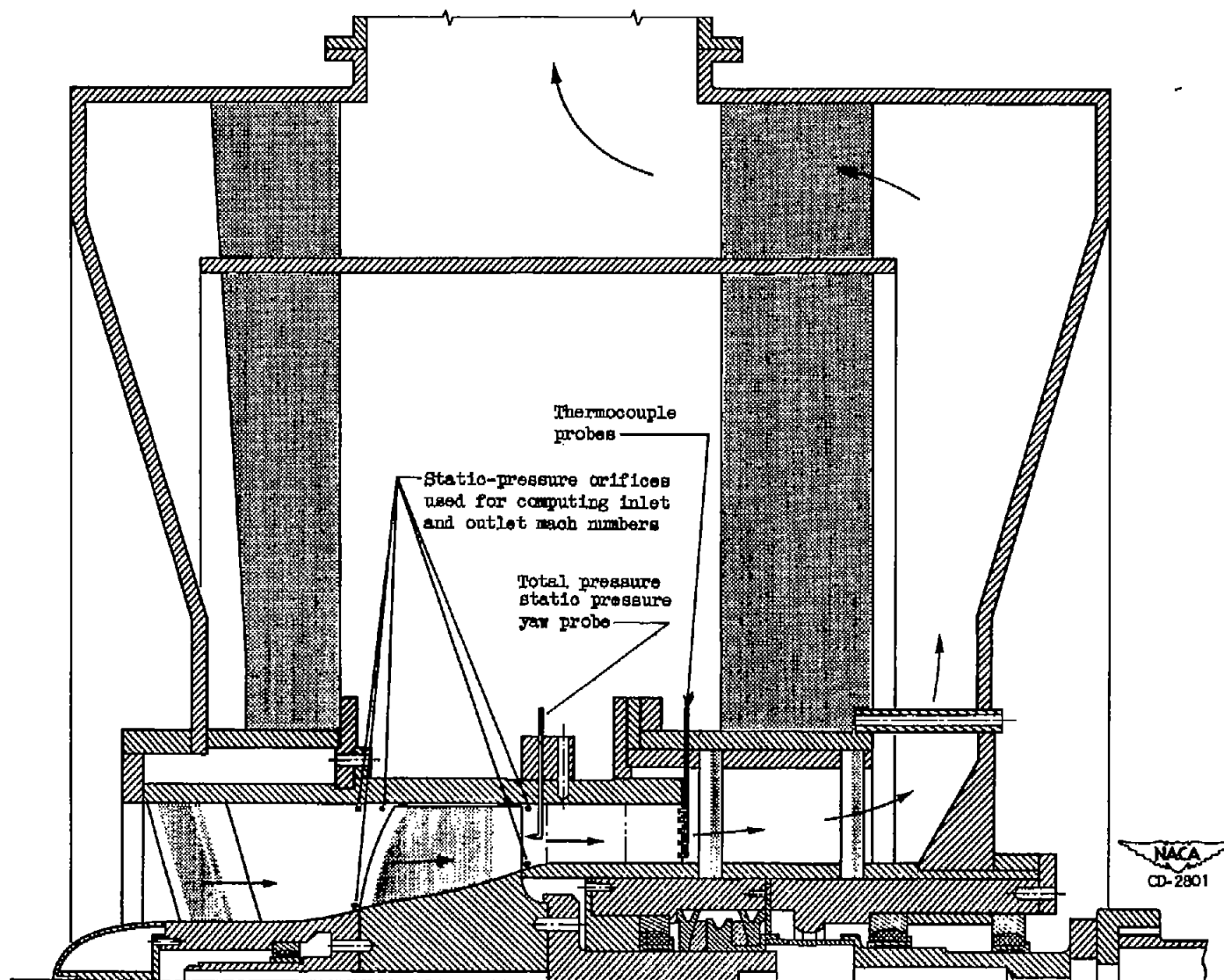


Figure 5. - 12-inch transonic compressor test rig.

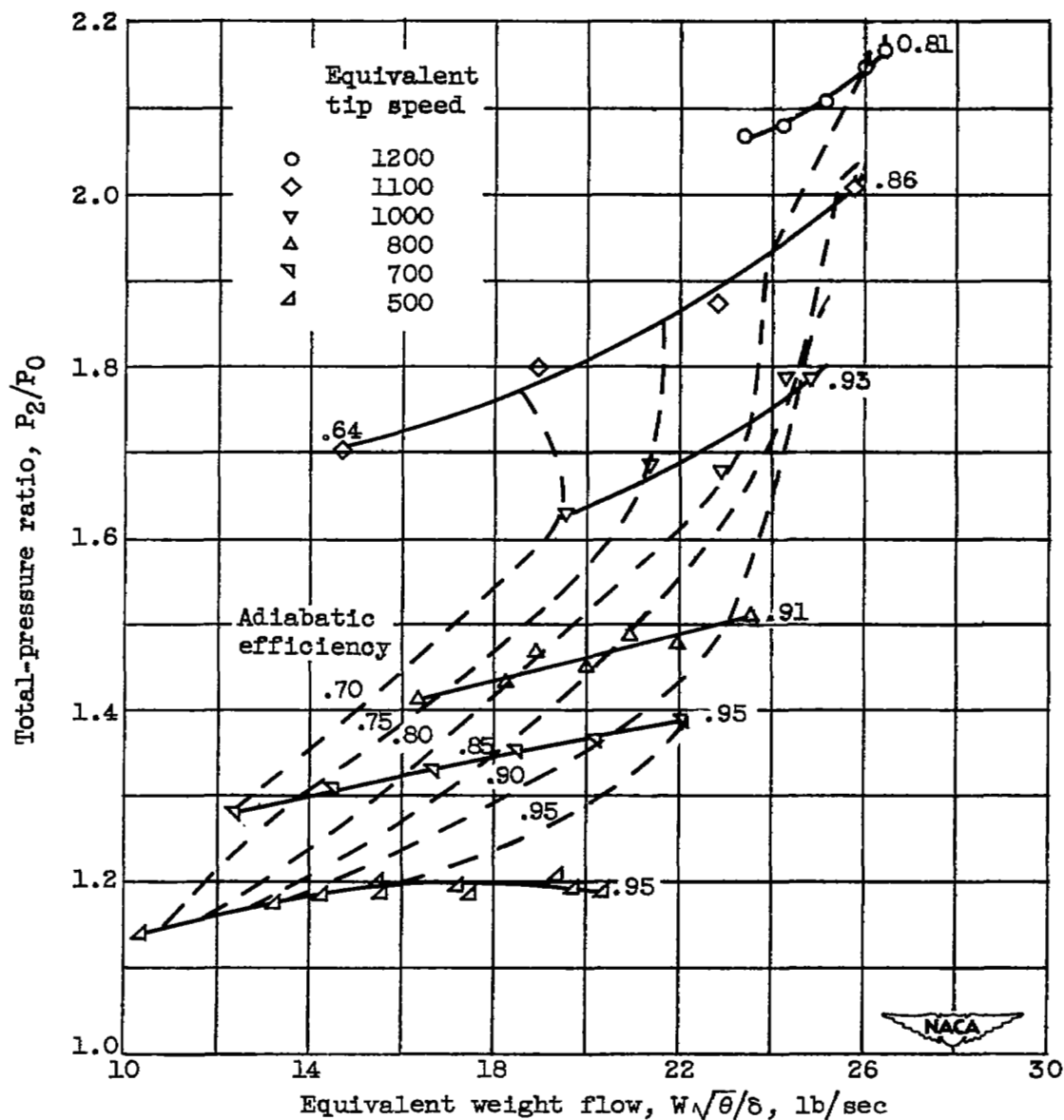


Figure 6. - Over-all performance of transonic mixed-flow impeller.

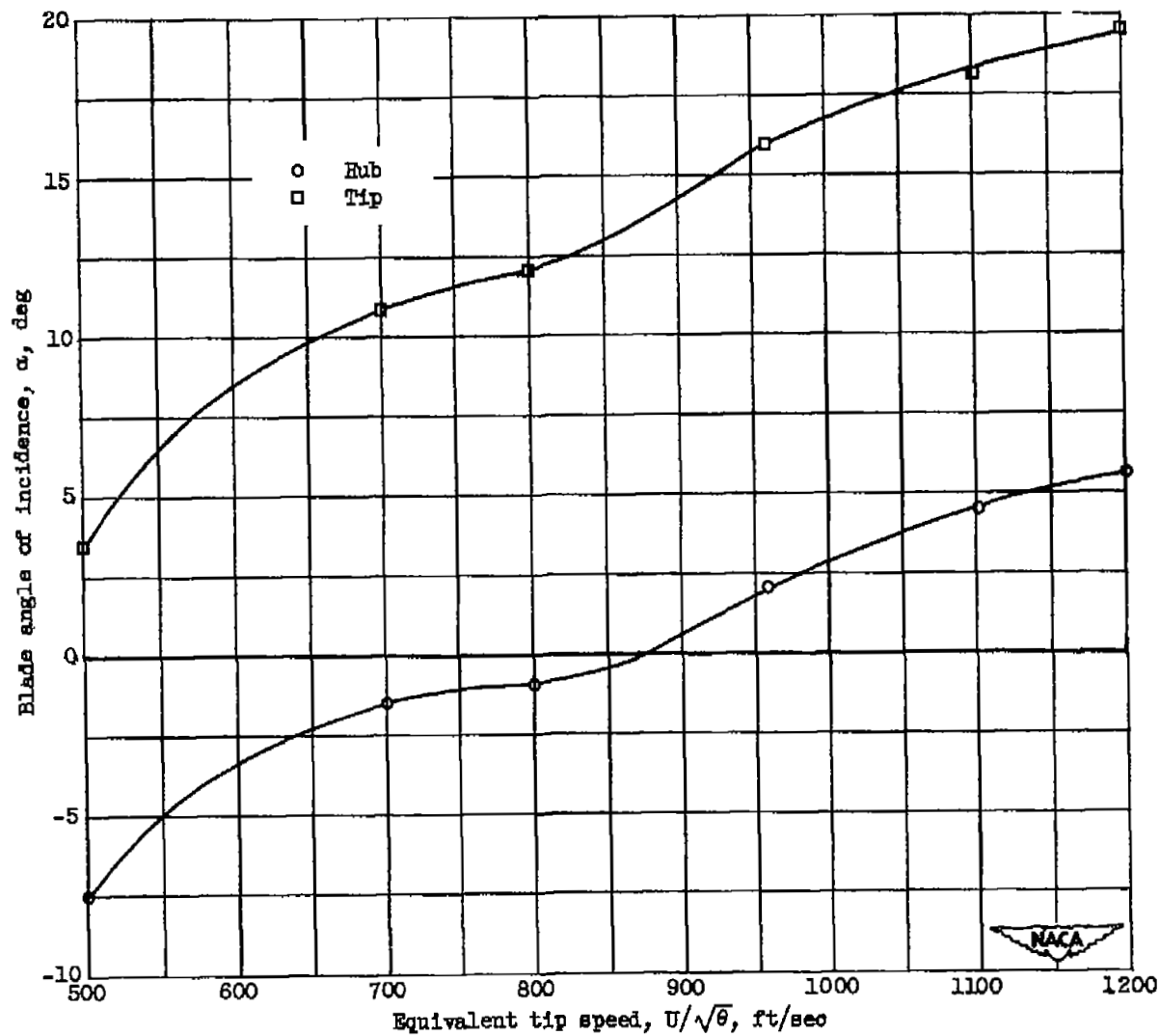


Figure 7. - Variation of hub and tip angle of incidence with impeller tip speed for minimum back pressure condition.

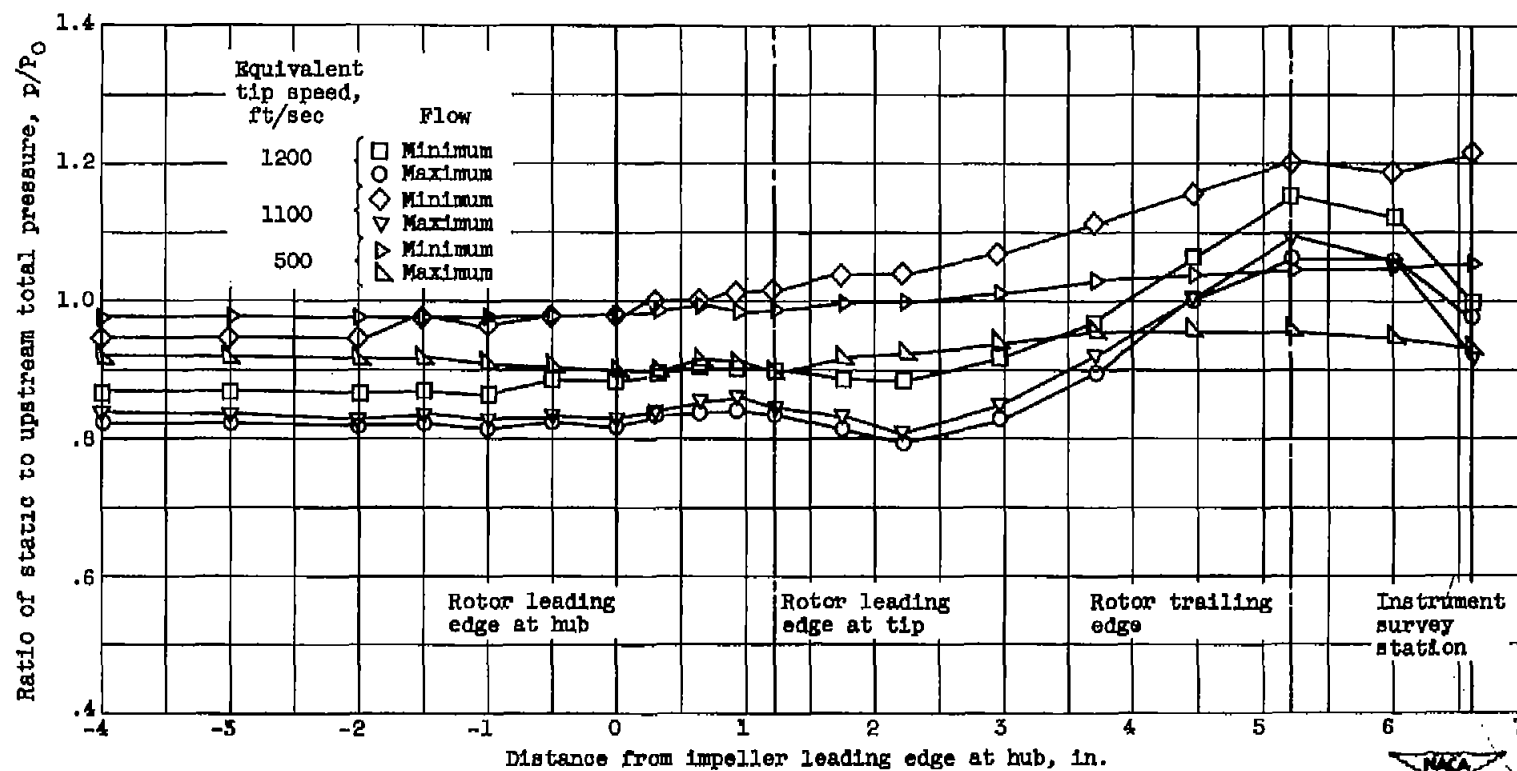


Figure 8. - Static-pressure distributions on outer casing for maximum and minimum flow at 500, 1100, and 1200 feet per second.

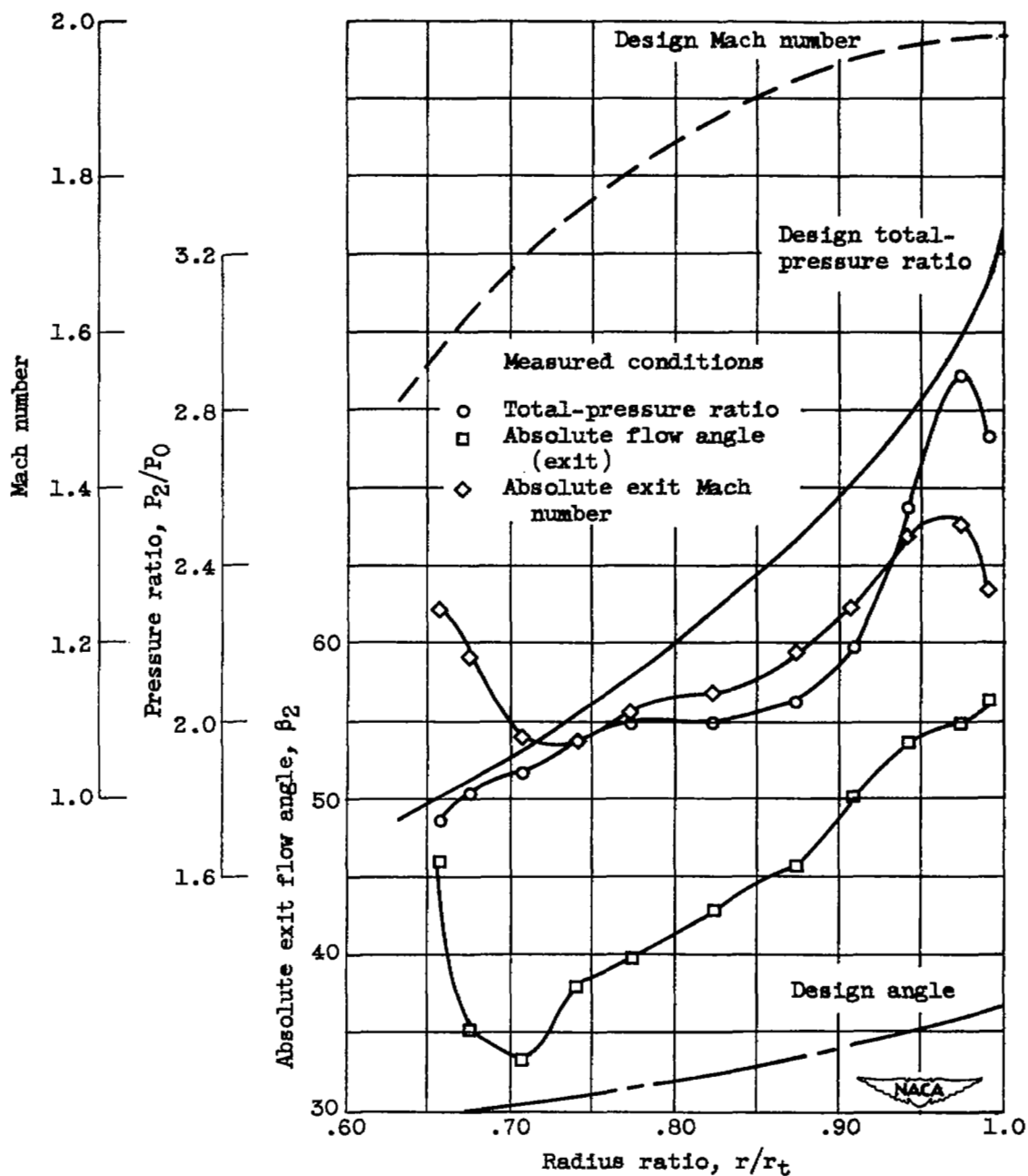


Figure 9. - Measured flow conditions at impeller exit for design speed and maximum weight flow.



Figure 10. - Transonic impeller after installation of damping wires.

~~SECURITY INFORMATION~~

~~XXXXXXXXXXXXXXXXXXXX~~



3 1176 01435 6795

~~XXXXXXXXXXXXXXXXXXXX~~